

UNCLASSIFIED

Defense Technical Information Center
Compilation Part Notice

ADP014044

TITLE: STAP Architectures and Limiting Effects

DISTRIBUTION: Approved for public release, distribution unlimited
Availability: Hard copy only.

This paper is part of the following report:

TITLE: Military Application of Space-Time Adaptive Processing [Les applications militaires du traitement adaptatif espace-temps]

To order the complete compilation report, use: ADA415645

The component part is provided here to allow users access to individually authored sections of proceedings, annals, symposia, etc. However, the component should be considered within the context of the overall compilation report and not as a stand-alone technical report.

The following component part numbers comprise the compilation report:

ADP014040 thru ADP014047

UNCLASSIFIED

STAP Architectures and Limiting Effects

Richard Klemm

FGAN-FHR, Neuenahrer Str. 20, D 53343 Wachtberg, Germany

Tel +49 228 9435 377; Fax +49 228 9435 618; email r.klemm@fgan.de

Abstract

Detection of slowly moving targets by air- and spaceborne MTI radar is heavily degraded by the motion induced Doppler spread of clutter returns. Space-time adaptive processing (STAP) can achieve optimum clutter rejection via implicit platform motion compensation. In this paper suboptimum receiver architectures are described. The impact of various radar parameters on the performance of STAP processors is demonstrated. Some aspects of jammer suppression will be touched on. The report concludes with an outlook on current and future research topics.

1 Suboptimum Processor Architectures

1.1 Pre-Doppler Techniques

1.1.1 Remarks on Clutter Subspace Techniques

In practice the space-time covariance matrix is not known but has to be estimated from received clutter data. Estimating and inverting the covariance matrix is commonly called the "sample matrix inverse" method (SMI). Due to its complexity SMI is of no value for most applications. It may also suffer from weak convergence in estimating the covariance matrix. There are several ways of reducing the computational workload and accelerating the convergence of adaption. Some of these techniques are listed here briefly. More details of several receiver architectures are given in the paper by WARD in this volume.

1.1.2 Rank reducing techniques

Rank reduction can be obtained by replacing \mathbf{Q}^{-1} in the optimum processor (see (19) in [30]) by a projection matrix orthogonal to the interference subspace (equ. 21 in [30]). Eigenvalue decomposition or Gram-Schmidt factorization are well-known tools. These subspace techniques show more rapid convergence than the SMI method. However, the computational load for filtering the actual data is not reduced since the order of the matrix is maintained (Ayoub [18]).

1.1.3 Order reducing techniques (pre-Doppler)

Order reducing technique reduce the signal and interference vector space before applying the SMI technique. Some of these techniques have been described by the author [26, Chapters 5-6, 9].

1.1.4 Space-Time Transforms

The original $N \times M$ vector space (N number of sensors, M number of echo pulses) is reduced by a linear transform. This transform may consist of the clutter eigenvectors obtained from a pre-calculated "typical" covariance matrix. Alternatively a bunch of beams can be formed so as to cover the whole azimuth range, each of them cascaded with a Doppler filter matched to the clutter Doppler in look direction. In both cases auxiliary channels are formed which are well matched to the interference. Both techniques have the disadvantage that the computational load increases with N and M . Moreover, they show little tolerance against channel errors and bandwidth effects.

Figure 1 shows the principle of the auxiliary channel processor (ACP). One recognoses the footprints of various search channels in the look direction (where the clutter maximum shows up) which differ in their target Doppler. Along the clutter spectrum one finds the footprints of auxiliary channels which point in different

directions and at different Doppler frequencies. A block diagram of the processor is shown in Figure 2. In Figure 3 it is demonstrated what happens if the number of channels is reduced below the wellknown rule $N_E = N + M - 1$. Just a small reduction from 48 down to 40 channels results in a strong degradation of the detectability of low Doppler targets. In conclusion, space-time transform architectures are still quite costly and may not be the optimum solution.

1.1.5 Spatial Transforms: Simplification in the Spatial Dimension

Spatial transforms can be obtained by forming subarrays to reduce the number of antenna channels (spatial dimension) and applying the SMI (or projection technique) at subarray level. Alternatively, a symmetric sidelobe canceller concept may be used. For certain antenna arrays configurations (especially linear, rectangular planar or, in general, horizontal cylindrical arrays) both techniques lead to near optimum clutter rejection performance at dramatically reduced computational expense.

For illustration consider Figure 4. It shows the evolution from a linear array via overlapping subarrays to a symmetric sidelobe canceller type of architecture. Notice, that in subfigure c. the sum above the dashed line includes all sensors which are common to *all* subarrays in b. In Figure 5 an implementation of planar patch arrays (rectangular, circular) is indicated. The black patches are part of the main beam while the white and the hatched patches form the auxiliary channels. Figure 6 shows the IF for the overlapping subarray processor according to Figure 4b. As can be seen, for two channels some degradation close to the clutter notch can be noticed. For higher numbers of channels the IF is nearly independent of the number of channels. This is a desirable property.

1.1.6 The Space-Time FIR Filter: Simplification in the Time Dimension

If the PRF is constant during the coherent processing interval space-time FIR filters can obtain near optimum clutter rejection at minimum cost. In conjunction with spatial transforms very efficient¹ space-time processors can be designed. The advantage of the FIR filter concept is that filtering can be accomplished in a pipeline mode as the echo pulses come in. The required number of calculations for filtering can be realised easily with nowadays digital technology. Because the temporal filter length can be very small the filter may be able to cope with non-stationarities caused by platform manoeuvres (s. RICHARDSON [36]) or staggered PRF by adaptation during the CPI.

Figure 7 shows the principle of a space-time FIR filter processor, details of the processor are given in Figure 8. In Figure 10 the clutter rejection performance of a FIR filter processor with the optimum space-time processor is compared. The FIR filter processor almost reaches the performance of the optimum processor, except for a small integration loss in the passband which is due to the shortening of the data sequence. The FIR filter must not slide over the edges of the data record, therefore the number of available data reduces to $M - L + 1$ where M is the number of echoes and L the number of temporal filter coefficients.

Figure 9 shows a processor architecture according to Figure 5c (symmetric auxiliary channel processor). The performance of this processor combines the properties of an overlapping subarray processor discussed before with those of the FIR filter.

A FIR filter processor is based on the assumption that the clutter echoes are stationary. This requires in particular that the PRF is constant. If the PRF is not constant because of staggering the FIR filter becomes time dependent. That means, the filter coefficients have to be adapted with each (irregular) pulse repetition interval (KLEMM [29]). The space-time submatrix chosen for calculating the FIR filter coefficients have to be selected for each PRI anew. Figure 11 illustrates how the sliding covariance submatrices relate to the total $N \times M$ (or $K \times M$) covariance matrix. The fat lines indicate which submatrix is associated with a certain step of the filter operation.

¹minimum number of space-time filter coefficients: 4

Figure 12 shows a numerical example. Notice that the abscissa extends between $-2B_c \dots 2B_c$ (four times the clutter bandwidth). Figure 12a shows the Doppler response of a space-time FIR filter with constant coefficients used an echo sequence with constant PRI. Ambiguous clutter notches can be noticed. In Figure 12b we used a pseudorandom stagger code. The plot shows the IF achieved by the optimum processor when the PRI is staggered. The ambiguities are removed at the expense of a slight decrease in IF and a little ripple close to the clutter notch. Applying a FIR filter to clutter data with staggered PRI leads to heavy losses in IF (Figure 12c). Matching the FIR filter coefficients to the stagger code by readapting at each PRI gives a reasonable clutter suppression (Figure 12d). The loss compared with the optimum processor (Figure 12b) is about 3 dB. The width of the clutter notch is slightly broadened.

1.1.7 Temporal FIR Filtering after Data Projection

Figure 14 shows the output signals of a moving array due to a stationary source (clutter patch) which causes a spatial frequency across the array. This frequency corresponds to the direction of the source. As can be seen the frequency modulation is fixed in space while the array is moving. The array spacing and the PRF can be chosen in such a way that all signals projected onto a common time axis form an equidistant time series (see the lowest subfigure). For clutter the frequency is bandlimited according to the spatial limits in azimuth $\vartheta \dots 180^\circ$. For a moving target higher frequency components occur as can be seen in Figure 15. It is obvious that clutter rejection can be carried out by a simple high pass filter.

1.2 Post-Doppler Techniques

1.2.1 Frequency domain (post-Doppler) approaches

There are several ways of performing interference cancellation in the frequency domain [46], [26, Chapter 9].

1.2.2 Spatial and Doppler Transforms

The Auxiliary Sensors/Echo Processor (ASEP) applies the symmetric auxiliary sensor principle according to Figure 4c in both the spatial and temporal domains, see Figure 13. Now we have $K - 1$ auxiliary sensors (top of figure) and $L - 1$ auxiliary echoes (the white parts in the memory). It can be shown that this processor is very close to the optimum.

1.2.3 Frequency-Dependent Spatial Processing

If the CPI is long (several hundreds of echoes) like for instance in SAR applications the correlation among frequency channels becomes asymptotically zero so that the space-frequency covariance matrix becomes block diagonal. This property can be exploited to reduce the computational cost by omitting spectral cross-terms. Then one ends up with spatial SMI for all individual frequencies. In conjunction with a spatial transform technique this kind of processor can be very efficient. A block diagram is given in Figure 16. Notice that this processor works only for long data sequences as may occur in SAR or HPRF radar whereas the ASEP (see previous section) works independently of the number of echoes. For more details see WARD [46] and KLEMM [26, Chapter 9].

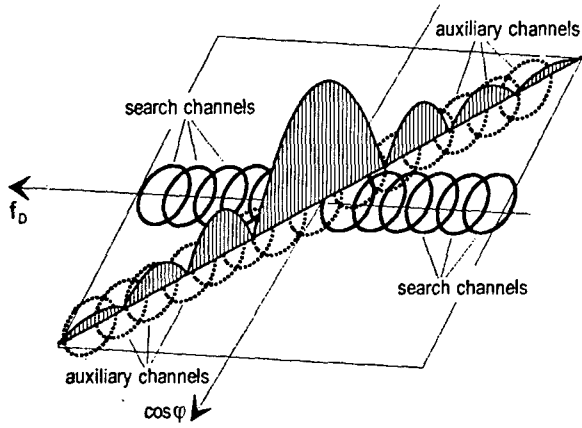


Figure 1: Principle of the auxiliary channel processor (ACP)

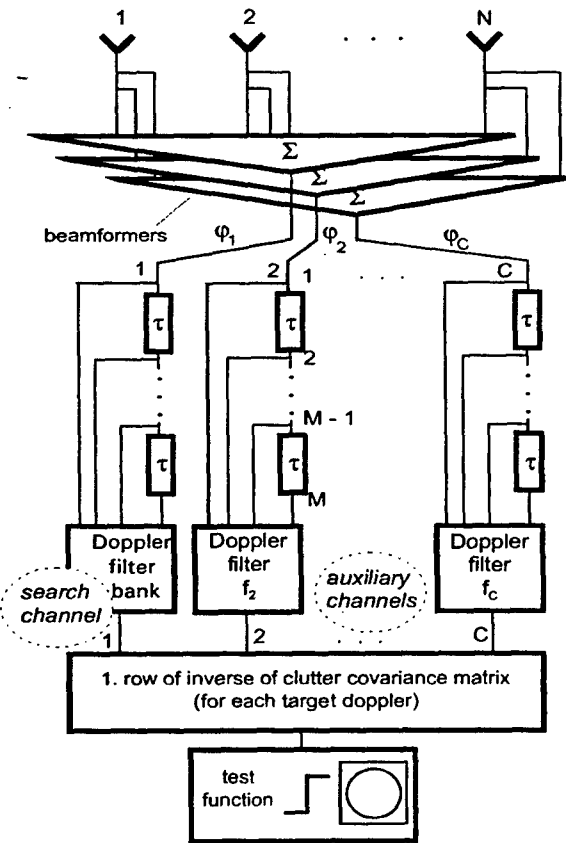


Figure 2: Block diagram of the auxiliary channel processor (ACP)

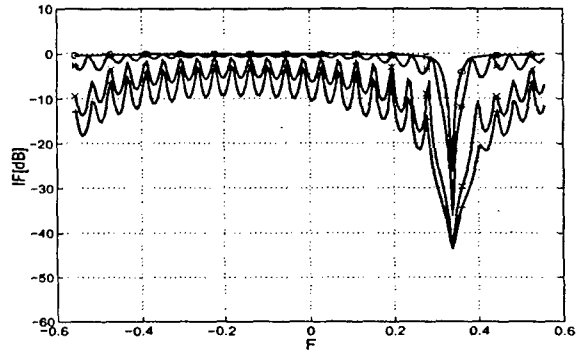


Figure 3: Reduction of the number of channels (FL, ACP): $\circ C = 48$; $* C = 40$; $\times C = 32$; $+ C = 24$

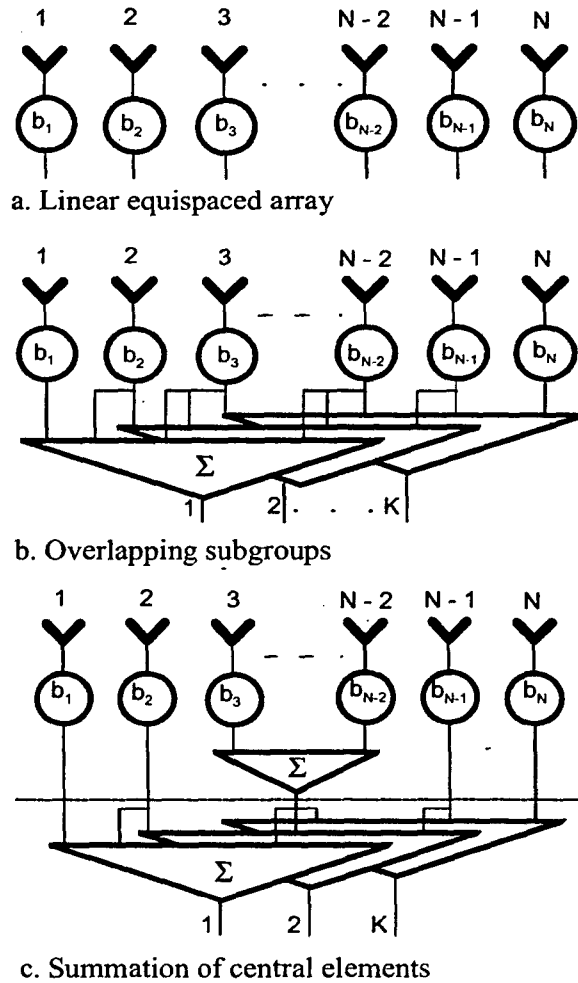


Figure 4: From subarrays to auxiliary elements

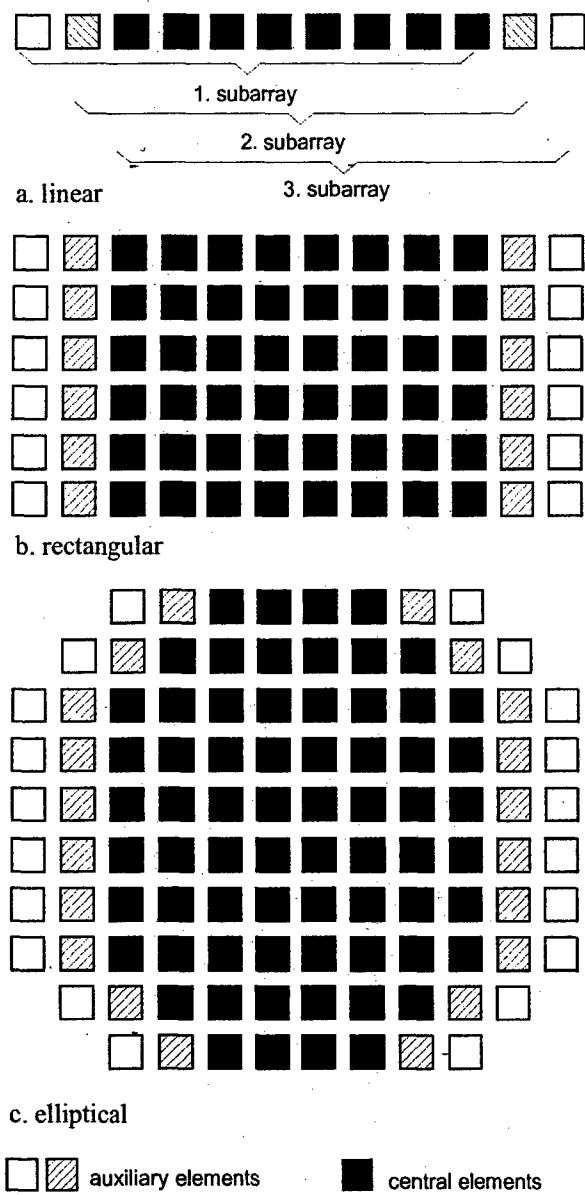


Figure 5: Clutter optimized planar array antennas

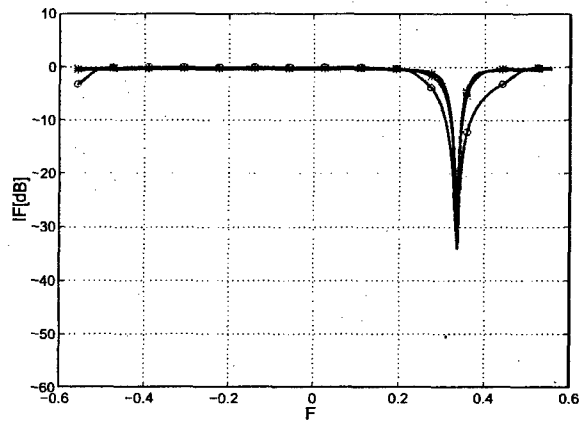


Figure 6: Influence of the number of channels (OUS, FL): $\circ K = 2$; $* K = 4$; $\times K = 6$; $+ K = 8$

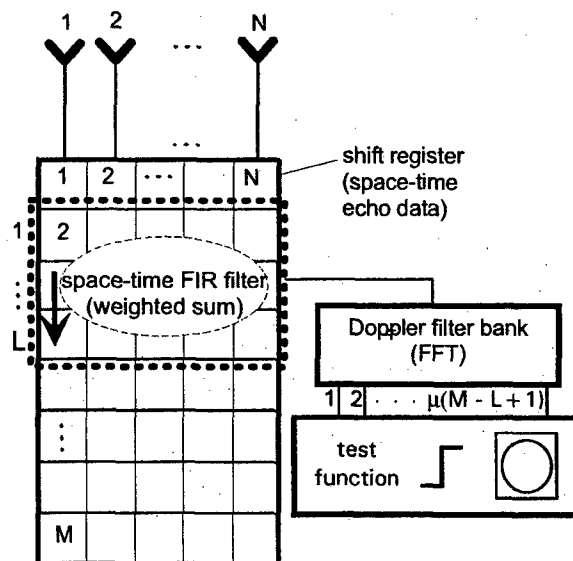


Figure 7: Space-time FIR filter processor

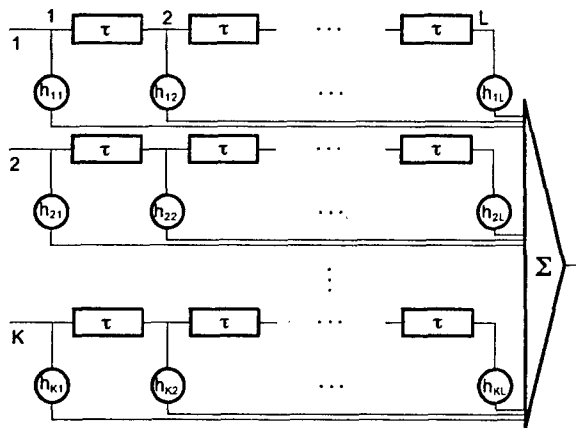


Figure 8: Detailed block diagram of the space-time FIR filter

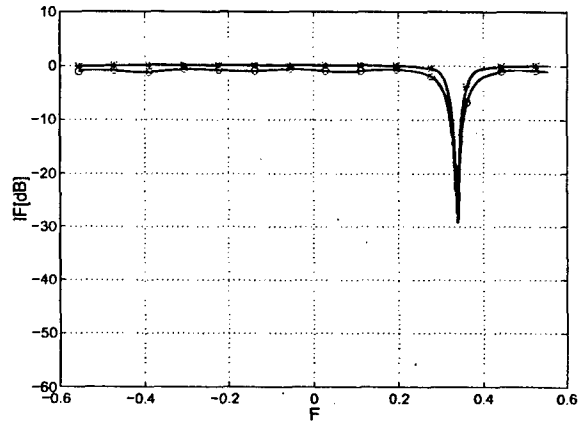


Figure 10: The FIR filter processor (full array, FL): o FIR filter processor ($L = 5$); * fully adaptive optimum processor

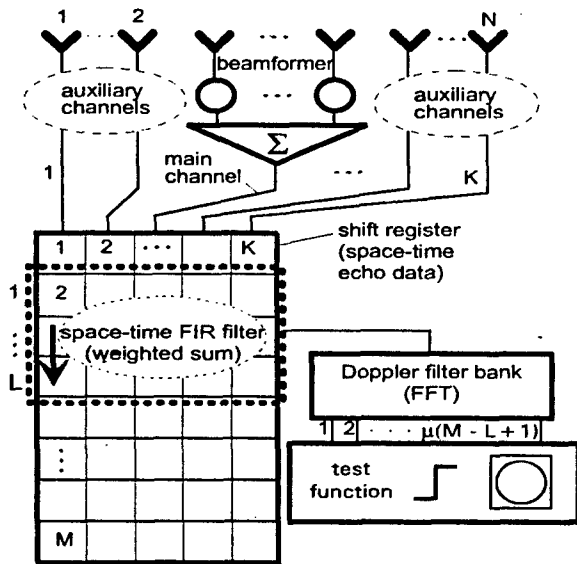


Figure 9: Space-time FIR filter processor with auxiliary element architecture

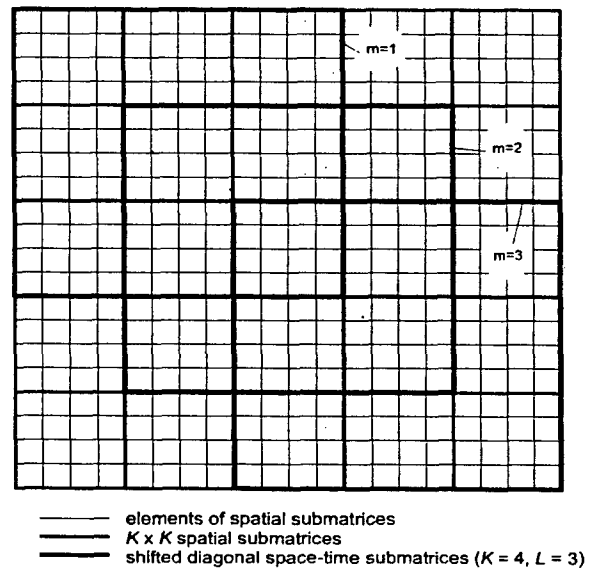


Figure 11: Matrix scheme for space-time FIR filtering, $K=4, M=5$

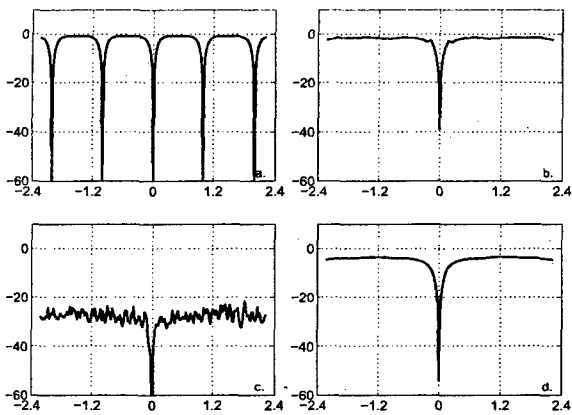


Figure 12: FIR filter with staggered PRI (pseudorandom stagger code, $\epsilon = 0.3$, PRF=3000 Hz, overlapping subarrays). a. no staggering; b. optimum processor with staggered PRI; c. fixed FIR filter with staggered PRI; d. FIR filter with variable coefficients and staggered PRI

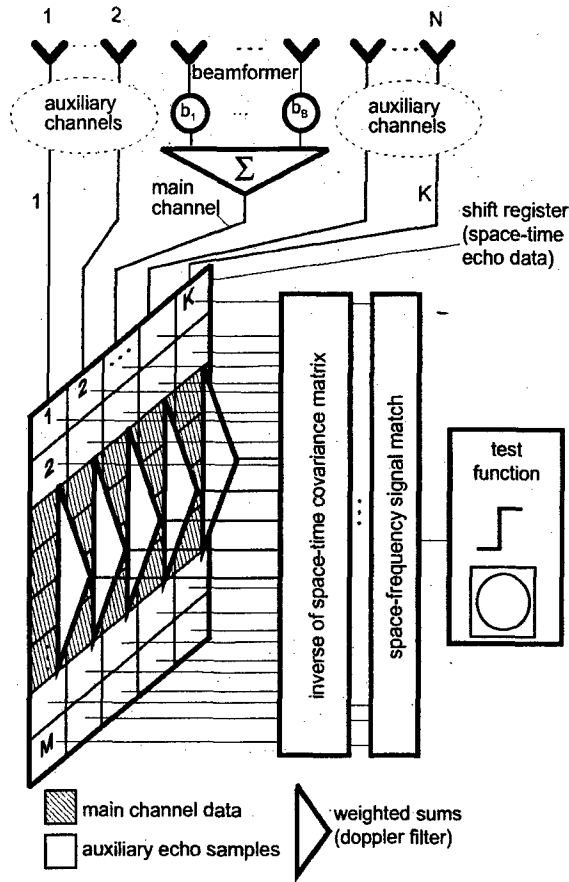


Figure 13: 2-D symmetric auxiliary sensor/echo processor (ASEP)

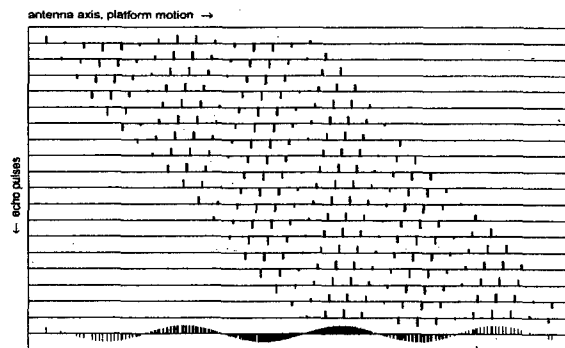


Figure 14: Projection of space-time echo samples onto a common time axis: clutter

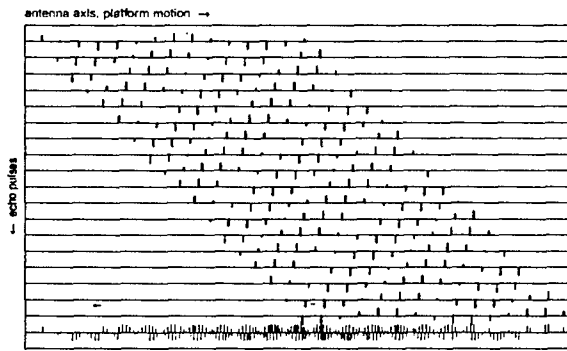


Figure 15: Projection of space-time echo samples onto a common time axis: Doppler target

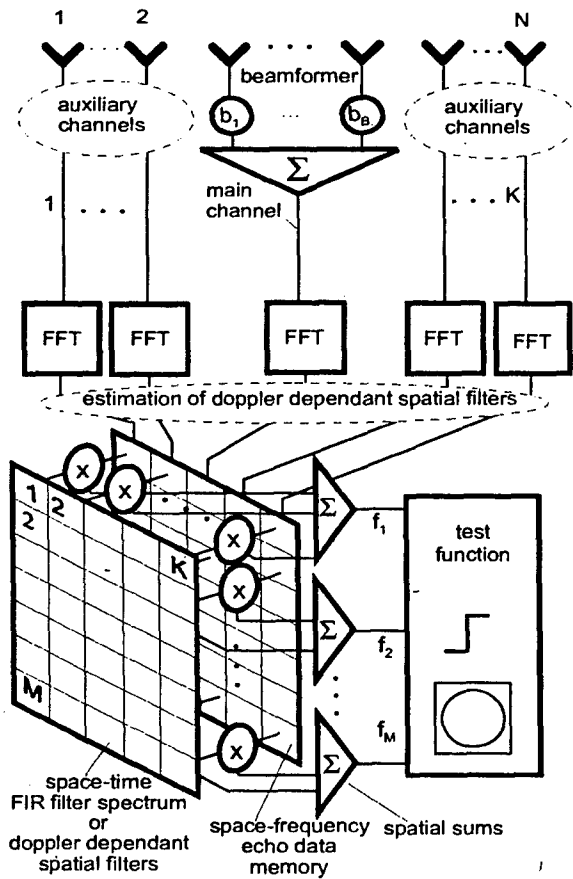


Figure 16: Frequency dependent spatial filter (FDSP)

2 Degrading Effects

2.1 Environmental Effects

2.1.1 Clutter Fluctuation

Internal clutter fluctuations (due to wind or sea state) cause a *temporal* (pulse-to-pulse) decorrelation of clutter echoes. This results in broadening of the clutter spectrum. The effect of clutter fluctuations on the clutter spectrum is shown in Figure 17 for a sidelooking array. Similar results can be expected for a forward looking array.

2.2 Radar Parameters

2.2.1 Effect of System Bandwidth

The system bandwidth causes a *spatial* decorrelation due to travel delays of incoming waves across the array. Therefore, this kind of decorrelation depends on the angle of arrival. It is maximum at endfire and zero at broadside. Moreover, it has been shown that this decorrelation effect does not occur for a sidelooking array. In case a sidelooking array the travel delays are compensated for by the DPCA property (KLEMM & ENDER [22]).

Figure 18 shows the effect of system bandwidth (rectangular frequency response) on the forward looking clutter spectrum. It can be noticed that the spectrum is broadened. The broadening effect is minimum at broadside ($\varphi = 0^\circ$) and becomes maximum towards endfire ($\varphi \pm 90^\circ$).

2.2.2 Effect of Range Walk

Range walk is another effect which can lead to temporal decorrelation of space-time clutter echoes. The influence of range walk on space-time clutter covariance matrices and the associated power spectra has been analysed by KREYENKAMP [33]. The principle of range walk due to radar platform motion is illustrated by Figure 19. It shows two rings of width $R_o - R_i$ which are shifted by

$$d = v_p m T \quad m = 1 \dots M \quad (1)$$

which is the distance the radar passes during the time mT . Both rings denote range bins as seen by the radar at different instances of time.

With the usual assumption that the clutter background consists of a large number of spatially uncorrelated scatterers we can conclude that the correlation between the two instances of time is given by the area where both range rings overlap

$$\rho_{mp}(\varphi) = \frac{\delta_{m-p}(\varphi)}{\Delta_R} \quad m, p = 1 \dots M \quad (2)$$

with $\Delta_R = R_o - R_i$ denoting the width of the range bin. Notice that, opposite to decorrelation by internal clutter motion, the decorrelation due to range walk is azimuth dependant. Obviously the correlation is maximum in the broadsight direction of a sidelooking array (SL) and minimum in forward looking direction (FL).

The distance $\delta(\varphi)$ can be calculated as follows

$$\delta(\varphi) = \sqrt{(x_P(\varphi) - x_Q(\varphi))^2 + (y_P(\varphi) - y_Q(\varphi))^2} \quad (3)$$

where x_P, y_P and x_Q, y_Q are the coordinates of the points P and Q in Figure 19 which can be obtained from simple geometrical relations.

It should be noted that in practice the temporal decorrelation effect due to range walk will be even stronger than described above. The received signal passes normally a bandwidth limiting matched filter so that the output signal is the autocorrelation function of the transmit signal. In case of range walk the individual shape of the matched filter response causes additional decorrelation which depends on the shape of the transmitted

waveform. In the subsequent discussion we omit this aspect and assume that the matched filter response is constant across the range bin.

Figure 20 shows a clutter power spectrum for a forward looking linear array. The effect of range walk can be noticed as ridge in the look direction, i. e., the direction of the transmit beam (here: $\varphi = 45^\circ$). This ridge means, however, a broadening of the spectrum in look direction and, hence a broadening of the associated clutter notch, which in turn means some degradation in low Doppler target detection.

2.2.3 Doppler Spread in Range Gate

For narrowband, i.e., low range resolution radar the range bins may be so large that a Doppler spread inside the range gate becomes significant. This effect will occur only if the clutter Doppler is range dependent, that means, for antenna configurations other than sidelooking. It is shown in Figure 21 (forward looking linear array) that for very low range resolution the Doppler spread effect dominates (a.), that there is an optimum at medium resolution (b.) and for higher resolution the range walk effect dominates (c. and d.).

2.3 Radar Ambiguities

By choosing a certain PRF Doppler and range ambiguities are determined. The effect of both Doppler and range ambiguities is discussed in the sequel.

2.3.1 Doppler Ambiguities

Constant PRF leads to Doppler ambiguities which has two consequences. This means that a Doppler filter bank has an ambiguous frequency response (see upper subfigure in Figure 24) so that the target Doppler can only be estimated modulo PRF. Secondly, the clutter spectrum becomes ambiguous (s. Figure 22) so that ambiguous clutter notches occur (blind velocities). Doppler ambiguities can be avoided by pulse-to-pulse staggering. In Figure 23 we see for example pseudorandom stagger patterns. As can be seen the Doppler responses in Figure 22 become unambiguous, however at the expense of higher Doppler sidelobes. Space-time adaptive processing takes the stagger pattern into account. Figure 25 shows the same clutter spectrum as Figure 24, however with pseudorandom staggering. Except for a small ripple the ambiguities have been removed.

2.3.2 Range Ambiguities

If the pulse repetition frequency ($PRF = \frac{1}{T}$) is chosen so that the radar is range ambiguous the received clutter echo becomes a superposition of clutter components from different ranges. In case of sidelooking radar this does not cause severe problems because all the ambiguous clutter arrivals have the same Doppler frequency. In case of a forward looking radar, however, different arrivals exhibit different Doppler frequencies. This is illustrated in a range-Doppler map² as shown in Figure 26.

The bended curve denotes the trajectory of the primary clutter. Notice the range dependency of the clutter Doppler. The straight line on the right reflects the ambiguous clutter returns. They originate from larger ranges (or: smaller depression angles) and have, therefore, larger Doppler frequencies. It has been shown by the author that the ambiguous clutter portion can be cancelled by "vertical nulling" using a planar array which is adaptive in both dimensions (horizontal and vertical) [24].

Figure 26 shows the ambiguous response of a forward looking linear array. The second clutter notch on the right is due to range ambiguity. Figure 28 shows the same situation, however using a planar 2d adaptive array. As can be noticed the ambiguities have been cancelled.

²This map shows the improvement factor in signal-to-clutter ratio as obtained by optimum processing, s. Chapter 4

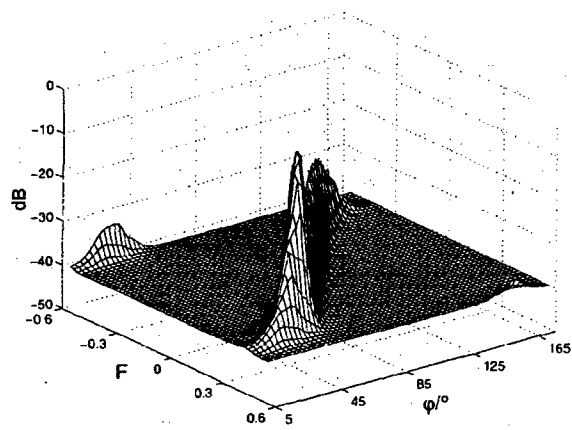


Figure 17: MV spectrum for sidelooking array ($B_c = 0.2$)

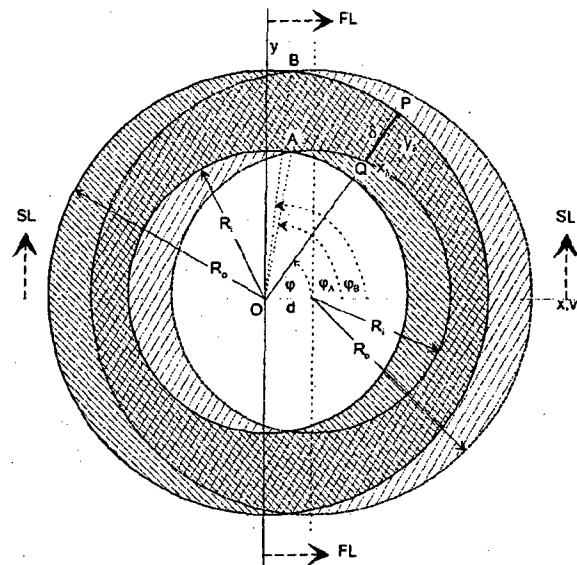


Figure 19: Geometry of range walk (©1999 AEU)

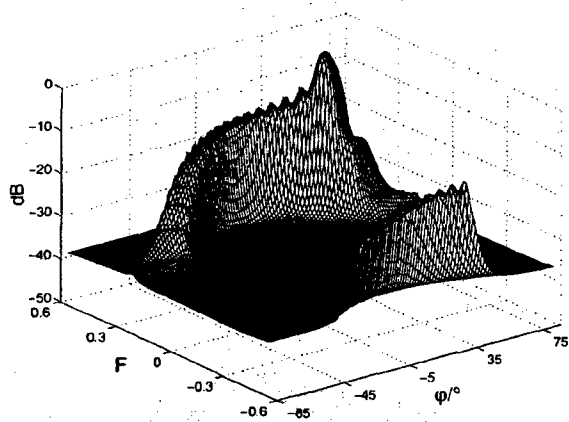


Figure 18: MV spectrum (FL array, rectangular frequency response, $B_s = 0.2$)

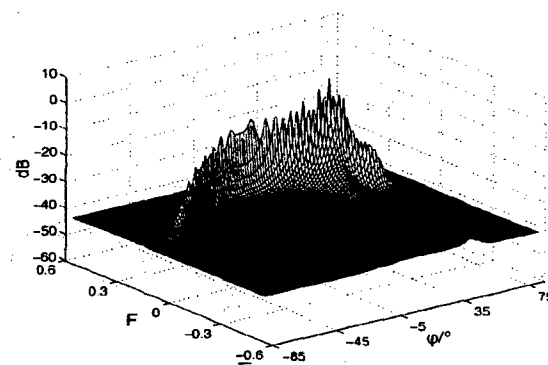


Figure 20: Clutter power spectrum (FL array) with range walk ($\Delta_R = 10m$)

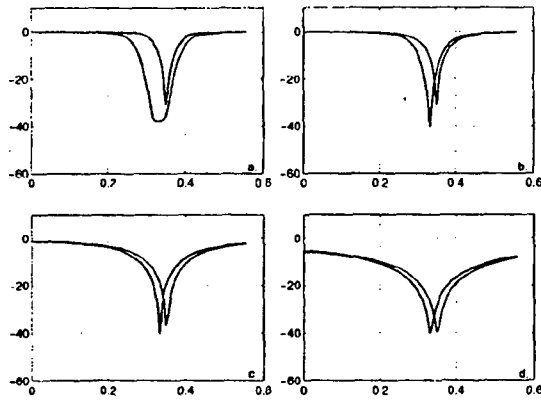


Figure 21: Doppler spread and range walk (IF vs F, FL, $H = 1$ km; left clutter notch: $R_s = 3$ km, right clutter notch: $R_s = 10$ km): a. $\Delta_R = 1500$ m; b. $\Delta_R = 150$ m; c. $\Delta_R = 15$ m; d. $\Delta_R = 1.5$ m

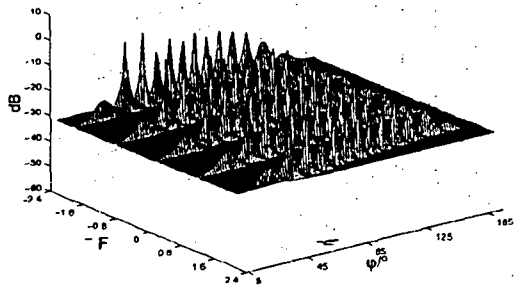


Figure 22: Azimuth-Doppler clutter spectrum without staggering

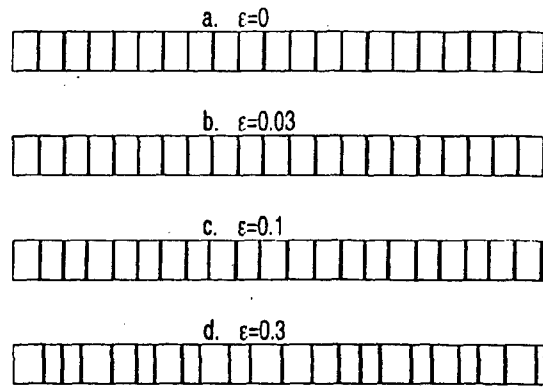


Figure 23: Pseudo-random stagger patterns

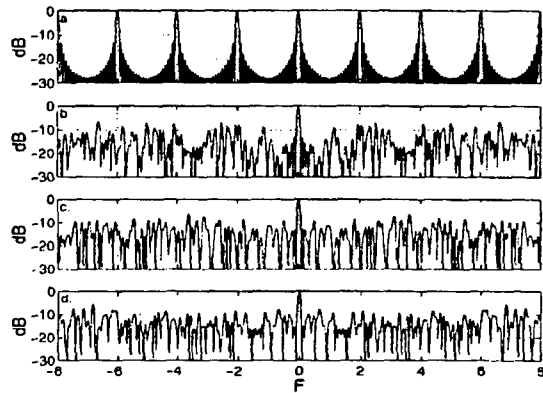


Figure 24: Doppler channel response for pseudo-random staggering: a. $\epsilon = 0$; b. $\epsilon = 0.03$; c. $\epsilon = 0.1$; d. $\epsilon = 0.3$

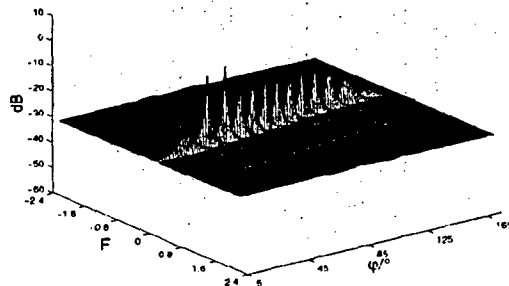


Figure 25: Azimuth-Doppler clutter spectrum with pseudo-random staggering

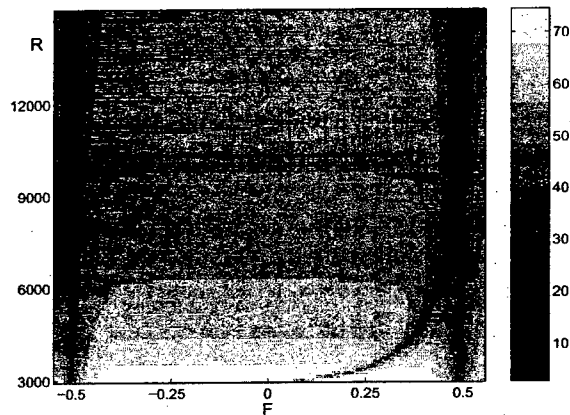


Figure 26: Range-Doppler Matrix (IF[dB] vs R/m and F; FL, $\varphi_L = 0^\circ$, PRF=Nyquist of clutter band)

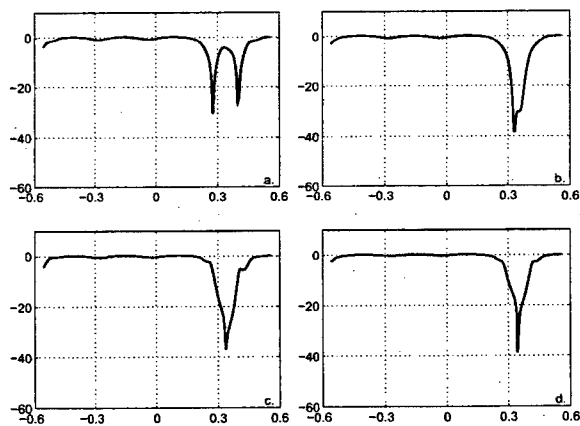


Figure 27: Influence of multiple-time around clutter (IF vs F; fully adaptive FIR filter processor, linear array, FL): a. $R_0/H = 1.66$; b. $R_0/H = 3$; c. $R_0/H = 4.33$; d. $R_0/H = 5.66$

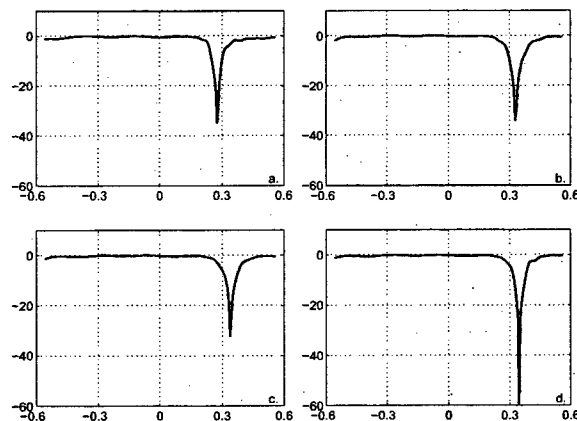


Figure 28: Influence of multiple-time around clutter (IF vs F; fully adaptive FIR filter processor, planar array with 6 rows of 24 elements each, FL, focused on the first range increment): a. $R_0/H = 1.66$; b. $R_0/H = 3$; c. $R_0/H = 4.33$; d. $R_0/H = 5.66$

3 Effect of Jamming

In this chapter the effect of additional jamming is discussed.

3.1 Characterisation of Jamming and Clutter

3.1.1 Eigenspectra

We assume broadband white noise jammers which cover the whole radar bandwidth. Let us first have a look at jammer eigenspectra. Let us assume an array with 24 elements and consider 24 echoes. Figure 29 shows eigenspectra of the space-time jammer covariance matrix for 1, 3, and 5 jammers. As can be seen each jammer produces 24 eigenvalues which is the number of echoes (the temporal dimension). This reflects that the jammers are white in the time dimension. In Figure 30 we see eigenspectra for superposition of clutter and the jammer scenario of Figure 29. Now we notice that each jammer adds $M = 24$ eigenvalues to the clutter eigenvalues.

3.1.2 Power Spectra

Figure 31 shows the well-known clutter spectrum for a sidelooking array and one additional jammer. It can be noticed that the jammer is white along the Doppler axis and discrete in azimuth. In Figure 32 we consider a clutter spectrum of a forward looking array according with 3 additional jammers.

3.2 Jammer and Clutter Suppression

We consider two cases, simultaneous jammer and clutter suppression and cascading spatial jammer cancellation with space-time clutter only rejection.

3.2.1 Simultaneous Processing

Figure 33 shows the improvement factor for the scenario given by Figure 31. We notice clearly the notches of jammer and clutter. An IF plot for the clutter-jammer scenario given in Figure 32 can be seen in Figure 34.

3.2.2 Cascading Jammer and Clutter Rejection

The principle is illustrated in Figure 35. Since the jammer is discrete in azimuth but white in Doppler it would be sufficient to apply standard *spatial* cancellation techniques to reject the jammer. Adaptation has to be done in a passive interval of the radar operation so that the anti-jamming filter is not corrupted by clutter. Then, in a subsequent space-time mode clutter is suppressed. The idea is that two cascaded filters might be less costly than one filter for simultaneous clutter and jammer suppression. Of course, adaptation of the clutter filter has to be done after the adapted anti-jamming filter. In Figure 35 the anti-jamming filter and the anti-clutter filter are shown schematically.

In Figure 36 a block diagram of a cascaded processor is shown. It should be noted that the fully adaptive anti-jamming filter can be replaced by a symmetric auxiliary sidelobe canceller scheme according to Figure 37 in order to further reduce the number of operations. Figure 38 shows the IF at the output of the adaptive anti-jamming filter for 3 active jammers. Figure 39 shows the clutter+jammer suppression performance of the cascaded processor for different numbers of jammers. Notice that the number of channels at the clutter rejection level is $K = 3$. The clutter notch can be seen clearly. The jammer notches are not visible because the jammer spectra are located in parallel to the Doppler axis (see for illustration Figure 40).

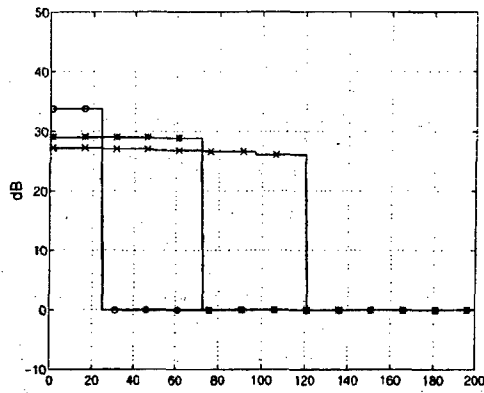


Figure 29: Space-time jammer eigenspectra (SL array): $\circ J = 1$; $* J = 3$; $\times J = 5$

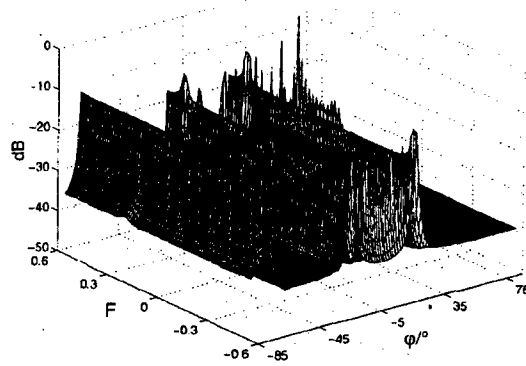


Figure 32: MV jammer+clutter spectrum (FL array, $J = 3$)

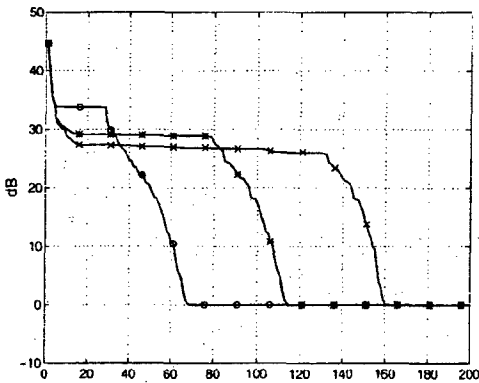


Figure 30: Space-time jammer+clutter eigenspectra (SL array) $\circ J = 1$; $* J = 3$; $\times J = 5$

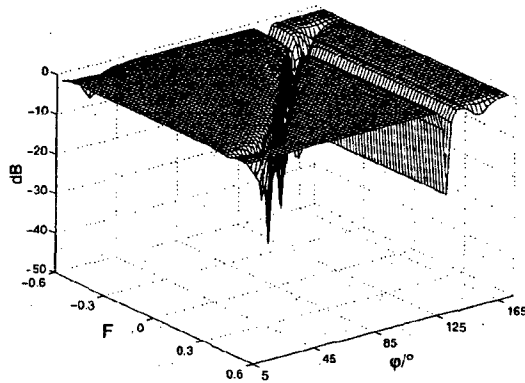


Figure 33: Improvement factor for a jammer+clutter scenario (SL array, $J = 1$)

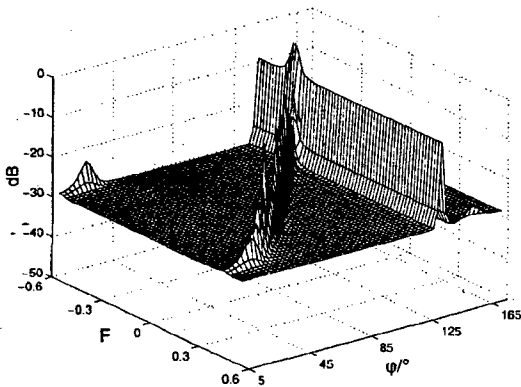


Figure 31: MV jammer+clutter spectrum (SL array, $J = 1$)

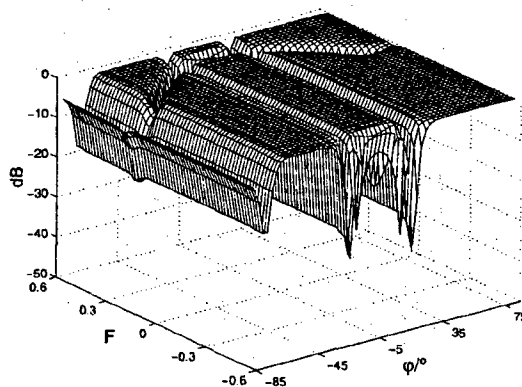


Figure 34: Improvement factor for a jammer+clutter scenario (FL array, $J = 3$)

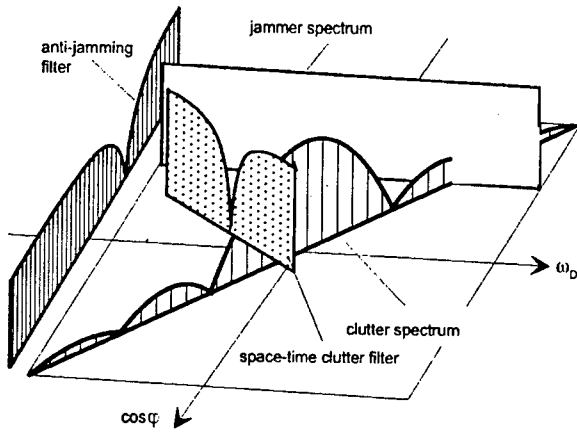


Figure 35: Cascading jammer and clutter filters

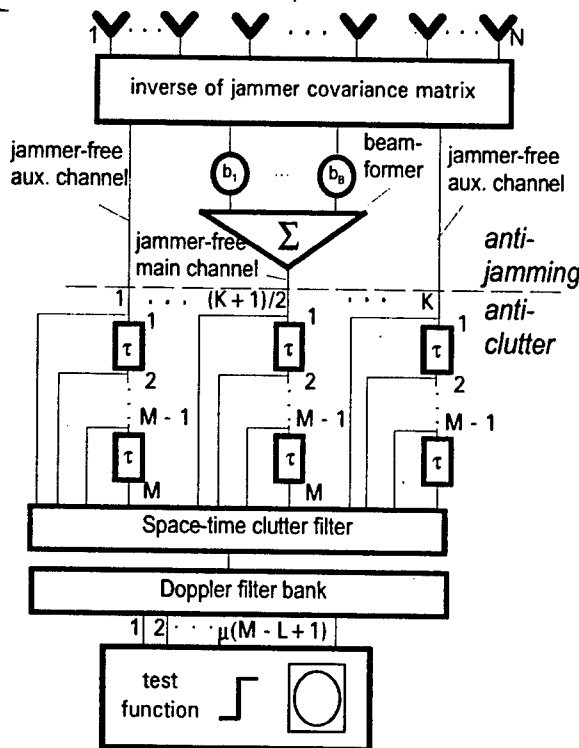


Figure 36: Cascading fully adaptive anti-jamming and auxiliary sensor clutter filters

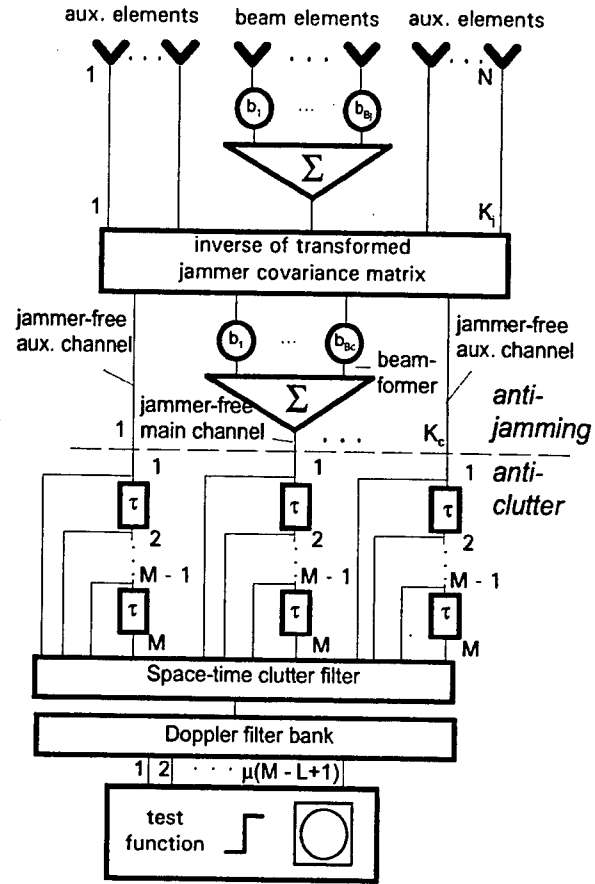


Figure 37: Cascading fully adaptive anti-jamming and auxiliary sensor clutter filters

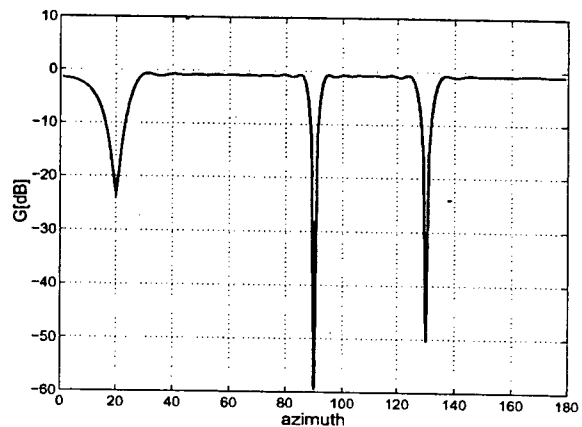


Figure 38: Performance of the anti-jamming processor

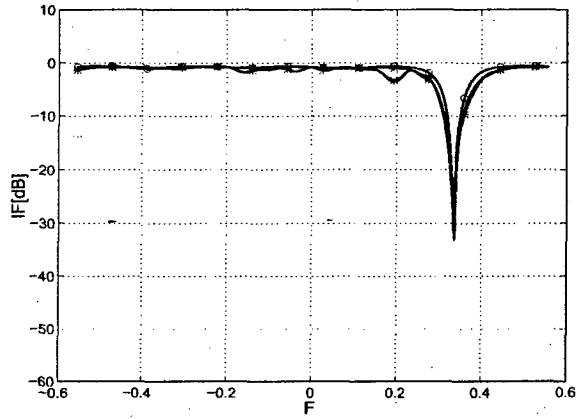


Figure 39: Optimum jammer suppression and auxiliary channel clutter filter cascaded ($N=25$, $K=3$, SL):
 $\circ J = 0$; $* J = 1$; $\times J = 2$; $+ J = 3$

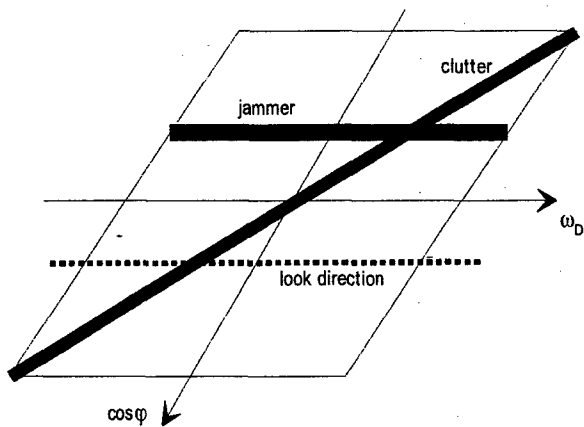


Figure 40: φ - ω_D trajectories of clutter and jammer (sidelooking array)

4 Current and Future Research Topics

4.0.3 STAP for Bistatic Radar

Bistatic radar operation has the advantage that the receiver cannot be located easily by hostile ESM techniques. The philosophy of bistatic radar for military operations is to design a cheap and/or remote transmitter and a displaced receiver with unknown position. Bistatic radar is much more complex in many respects than monostatic radar. In the following a few properties of bistatic STAP radar are briefly presented which differ from monostatic STAP radar.

4.0.4 Review of Monostatic Radar

Let us recall that for a sidelooking array the clutter Doppler is range independent. This follows from the fact that the array and the flight path coincide so that beam traces on the ground and isodops coincide (see Figure 41, receiver and transmitter being in the same location). The clutter trajectories in the azimuth-Doppler plane Figure 42 are straight lines along the diagonal of the azimuth-Doppler plot. Notice that for different ranges the same curves are obtained. The eigenspectrum (Figure 43) of a typical SL clutter covariance matrix follows the rule $N_E = N + M - 1$ (in this example $N=M=24$).

Figure 44 shows the same isodop plot as Figure 41, however for a forward looking array which means that the beamtraces are rotated by 90° . As can be seen there are a lot of intersections between isodops and beam traces which is an indication for the range dependence of the clutter Doppler. The clutter trajectories show circles whose radius is a measure for the range.

4.0.5 Impact of Bistatic Configuration

We focus on sidelooking arrays. Let us consider a certain bistatic configuration shown in Figure 46. Transmitter and receiver are separated and fly in different directions. Looking at the transmit beam traces a lot of intersections between beam traces and isodops can be noticed which tells us that the clutter Doppler is range dependent. This is also confirmed by the clutter trajectories in the azimuth-Doppler plane (Figure 47) which exhibit different shape for different range. Figure 48 shows a clutter power spectrum for the configuration shown in Figure 46. Comparing Figure 47 with Figure 42 or Figure 48 with Figure 42 shows that in bistatic configurations in general the clutter Doppler is range dependent. This has implications on the processing. Clutter rejection may require range dependent adaptation and filtering, and may suffer from shortage in training data. The eigenspectrum shows more than $N_E = N + M - 1$ clutter eigenvalues if no directive sensors are used. For directive sensors the eigenspectrum is very similar to the monostatic case (Figure 43).

In conclusion, sidelooking arrays have beneficial properties in monostatic operation (no clutter Doppler dependency with range) whereas in bistatic configurations this is not fulfilled. As stated before, bistatic configurations are more complex than monostatic ones. We find that this is also true for bistatic STAP operation. It appears, however, from the eigen- or power spectra that processor architectures will be similar to those used in monostatic operation.

4.0.6 Range and Doppler ambiguities

We found out that in bistatic radar configurations the clutter Doppler is range dependant even for a radar with *sidelooking* array. antenna. We can, therefore, expect that the multiple ambiguous returns which come from different ranges at different elevation angles will exhibit different Doppler frequencies.

Let us illustrate this by using Figure 50. Figure 50 shows IF curves versus target velocity for a sidelooking array in the bistatic configuration 2 (two aircraft on parallel flight paths). In Figure 50a the ideal case is shown. No range ambiguities have been assumed, and Doppler ambiguities do not occur inside the clutter band ($v_p = 90 \dots 90$ m/s) since the PRF has been chosen the Nyquist frequency of the clutter bandwidth (12000 Hz). In Figure 50b the PRF was chosen 4 times the Nyquist rate so that many range ambiguous clutter returns can

be expected. We notice a considerable broadening of the clutter notch³. Using a planar array with additional vertical adaptivity similar to section 2.3.2 compensates to a certain extent for the effect of ambiguous clutter returns so that the resulting clutter notch is narrowed (Figure 50c). Additional PRI staggering according to section 2.3.1 gives no difference since the clutter band is oversampled anyway with the chosen PRF.

4.1 Cramér-Rao Bounds

The next logical step after signal processing and target detection is target parameter estimation (range, Doppler, direction). These parameters are required for subsequent tracking algorithms. The Cramér-Rao bound (CRB) gives the lowest possible standard deviation of the estimated parameters. The CRB is associated with the optimum processor, however, for certain suboptimum techniques (those based on linear transforms, s. Chapter-5) the CRB can be calculated as well.

4.1.1 Optimum Processing

Figures 51 and 52 show the CRB for the optimum processor (Chapter 4) for azimuth and velocity estimation, respectively. The four curves have been calculated for different SNR. A flat clutter-free zone can be recognized. At the Doppler frequency where the processor is matched to the clutter the curves show a peak. This means that the standard deviation of the estimated parameter increases in the region of the clutter notch.

4.1.2 Impact of Radar Parameters

The CRB curves in Figure 53 have been calculated for different numbers of array elements (or: array apertures). It is obvious that the estimation error become larger as the array aperture becomes smaller. In Figure 54 the influence of spatial decorrelation due to the system bandwidth on the CRB is shown. This decorrelation leads to a broadening of the clutter power spectrum (see the example in Figure 18) and, hence to a broadening of the clutter notch of the associated adaptive clutter filter. This in turn means reduced detectability of low Doppler targets and a larger area with increased estimation error.

4.1.3 Suboptimum Transform Techniques

In Figure 55 some CRB curves have been plotted for the ASEP which is a very economic processor architecture (see section 5.2.1). This processor can be described by a linear transform (see [26, Chapter 9]). If the clutter process was multi-variate gaussian the transformed process is gaussian again so that an optimum processor can be designed at the transformed level and, hence, the CRB can be calculated for any type of transform processor. We notice from Figure 55 that the estimation error is slightly raised and the clutter peak is broadened. In conclusion, such transform techniques may achieve almost optimum clutter rejection and target detection performance. The estimation error, however, is more sensitive to such linear transforms.

4.1.4 Tracking with STAP radar

During a tracking phase the radar-target geometry changes with time. Target parameters such as azimuth, elevation, range and Doppler vary continuously.

This effect shall be illustrated by a simple scenario. Consider a slow target on the ground moving in parallel to the flight path of a fast airborne radar. Then one may get a SNIR response from the radar as shown in Figure 56.

Initially, the radar is behind the target. As the target is moving there is a difference in radial velocity determined by both the target and radar velocities. When the radar passes the target we obtain zero radial velocity for both the target and clutter. In this situation the target disappears in the clutter notch. After the radar has passed the target the target comes out of the clutter notch so that the SNIR increases again. After a while

³which in part is a consequence of the short duration of the coherent processing interval owing to the chosen PRF.

the target stops so that it behaves like clutter. As long as the target stops the SNIR is very low. As soon as the target accelerates again the SNIR increases rapidly. Notice that the SNIR is modulated by the sensor pattern while the radar is overtaking the target.

The problem of ground target tracking with a STAP radar has been discussed by KOCH and KLEMM [31]. It is shown in [31] how an intelligent tracking algorithm can exploit the specific properties of the signal output of a STAP radar.

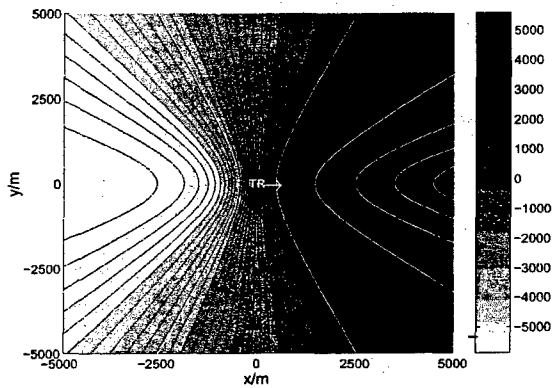


Figure 41: Isodops (black) and beam traces (white) for sidelooking linear array, monostatic (©1998 IEEE)

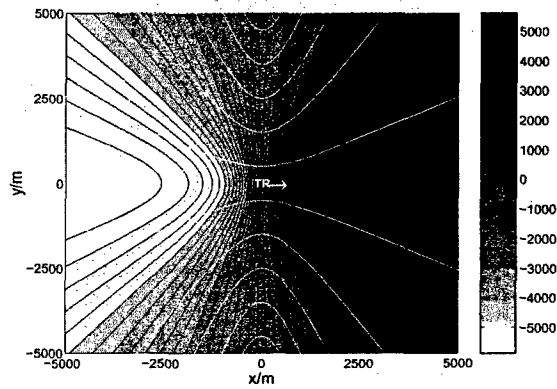


Figure 44: Isodops (black) and beam traces (white) for forward looking linear array, monostatic (©1998 IEEE)

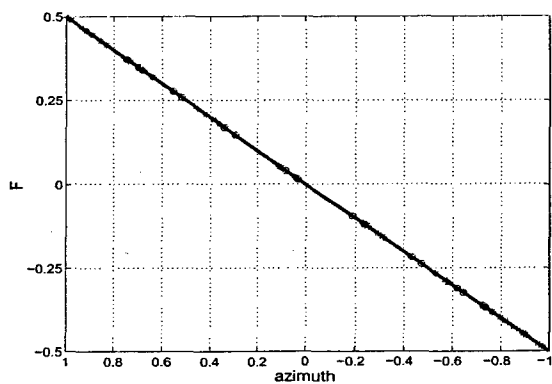


Figure 42: Azimuth-Doppler clutter trajectories (SL): $R = \circ 1 \text{ km}; * 2 \text{ km}; \times 4 \text{ km}; + 10 \text{ km}$ (©1998 IEEE)

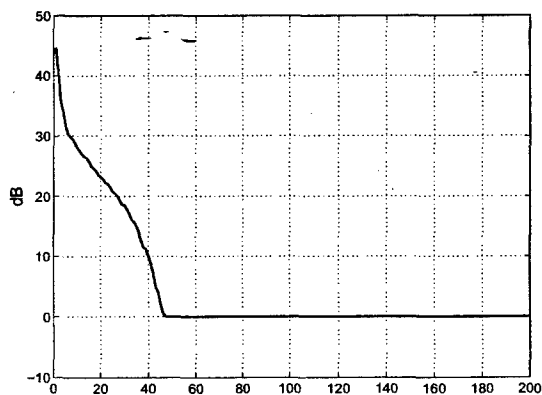


Figure 43: Clutter eigenspectrum (SL), (©1998 IEEE)

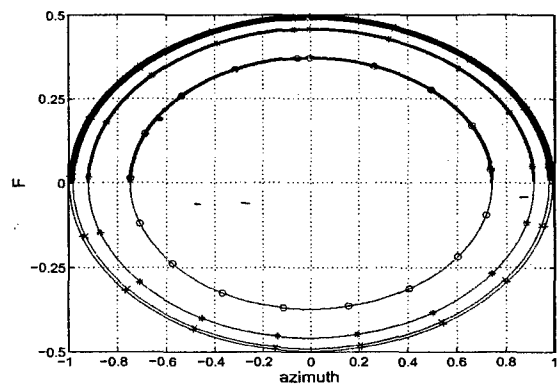


Figure 45: Azimuth-Doppler clutter trajectories (FL): $R = \circ 1 \text{ km}; * 2 \text{ km}; \times 4 \text{ km}; + 10 \text{ km}$ (©1998 IEEE)

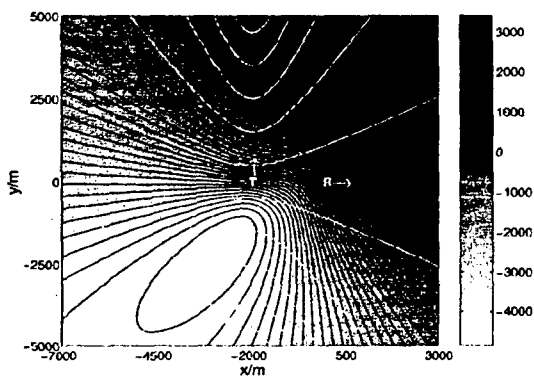


Figure 46: Isodops (black) and beam traces (white). SL, bistatic, (©1998 IEEE)

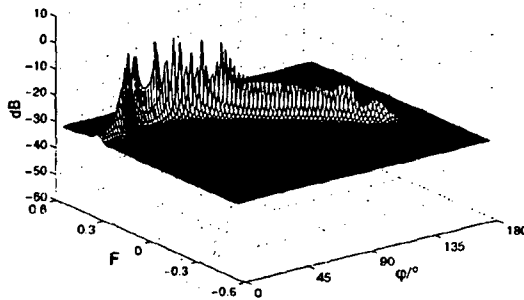


Figure 48: Clutter power spectrum (SL), bistatic (©1998 IEEE)

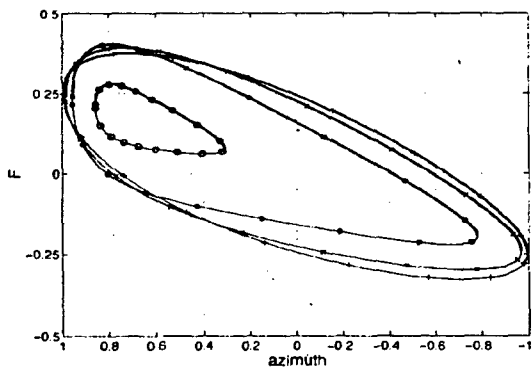


Figure 47: Azimuth-Doppler clutter trajectories (SL): R = o 1 km; * 2 km; x 4 km; + 10 km ($\delta_T = 90^\circ$), (©1998 IEEE)

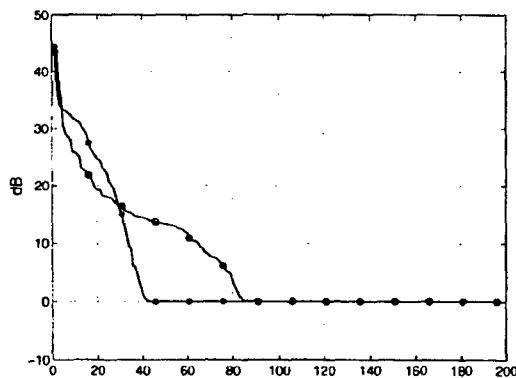


Figure 49: Clutter eigenspectrum (configuration as in Figure 46, SL), o omnidirectional sensor patterns; * directive sensor patterns, (©1998 IEEE)

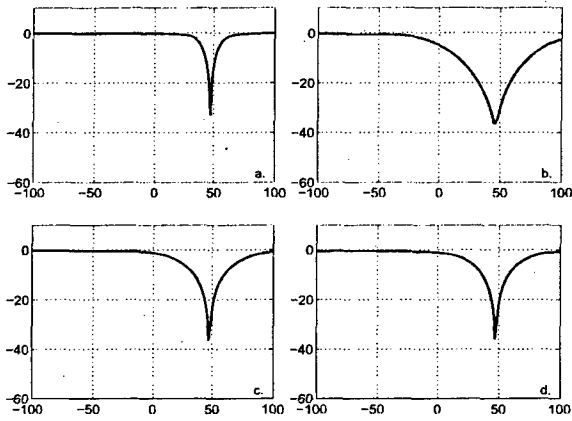


Figure 50: IF vs target velocity (m/s, sidelooking array, configuration 2, $R=10000$ m, $N=M=12$. a. PRF=Nyquist of clutter bandwidth, no range ambiguities; b. PRF= $4\times$ Nyquist, with range ambiguities; c. adaptive planar array; d. planar array + randomly staggered PRI

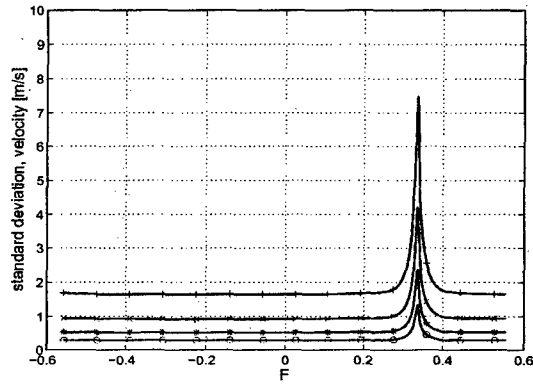


Figure 52: Effect of signal-to-noise-ratio on velocity estimation: SNR = \circ 10 dB; $*$ 0 dB; \times -10 dB; $+$ -20 dB

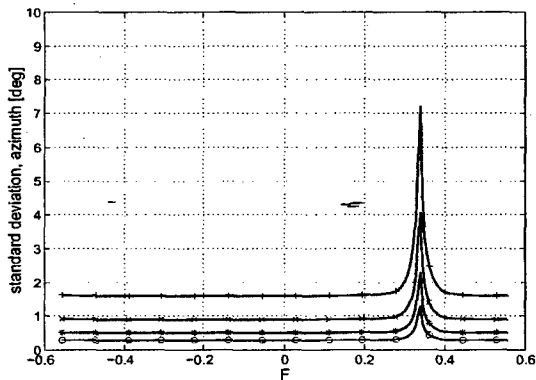


Figure 51: Effect of signal-to-noise-ratio on azimuth estimation: SNR = \circ 10 dB; $*$ 0 dB; \times -10 dB; $+$ -20 dB

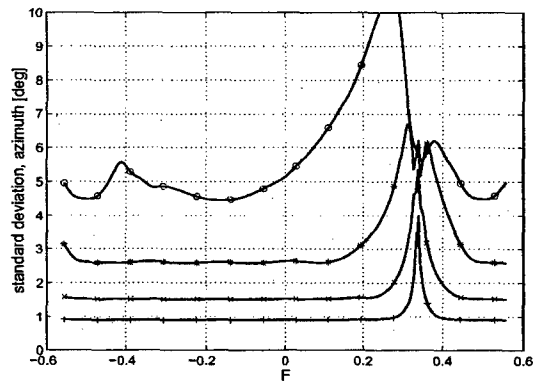


Figure 53: Impact of the array aperture size (azimuth estimation): $N = \circ$ 3; $*$ 6; \times 12; $+$ 24

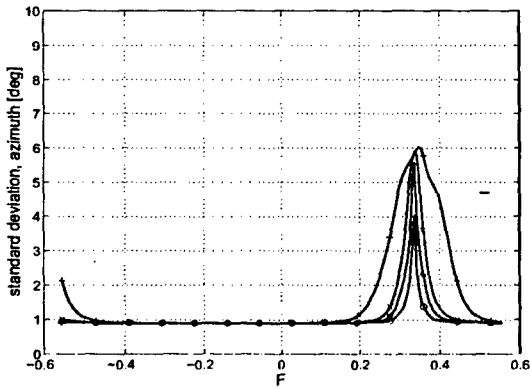


Figure 54: Effect of system bandwidth (FL): SNR =
 ○ $B_s = 0\%$; * $B_s = 1\%$; × $B_s = 5\%$; + $B_s = 30\%$

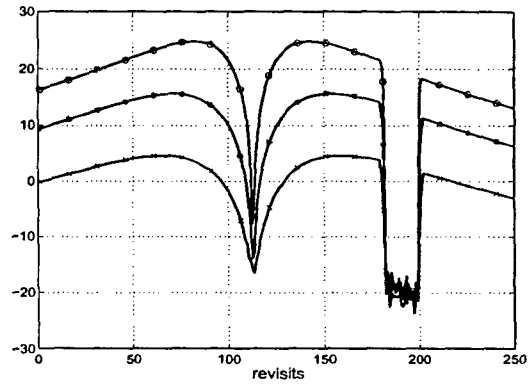


Figure 56: Optimum SNIR vs number of revisit for different system dimensions: ○ $N=M=24$; * $N=M=12$; × $N=M=6$

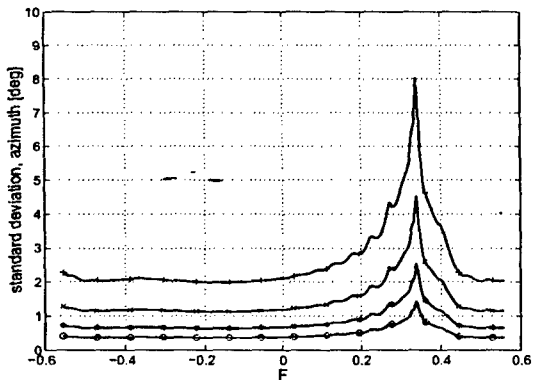


Figure 55: CRB for azimuth estimate (ASEP, $K = 5$, $L = 5$): SNR = ○ 10 dB; * 0 dB; × -10 dB; + -20 dB

References

- [1] Anderson, D. B., "A Microwave Technique to Reduce Platform Motion and Scanning Noise in Airborne Moving Target Radar", *IRE WESCON Conv. Record*, Vol. 2, pt. 1, 1958, pp. 202-211
- [2] Babu, S. B. N., Torres, J. A., Lamensdorf, D., "Space-Time Adaptive Processing for Airborne Phased Array Radar", *Proc. of the Conf. on Adaptive Antennas*, 7-8 November 1994, Melville, New York 11747, pp. 71-75
- [3] Brennan, L. E., Reed, I. S., "Theory of Adaptive Radar", *IEEE Trans. AES*, Vol. 9, No 2, March 1973, pp. 237-252
- [4] Brennan, L. E., Mallett, J. D., Reed, I. S., "Adaptive Arrays in Airborne MTI", *IEEE Trans. AP*, Vol. 24, No. 5, 1976, pp. 607-615
- [5] Brennan, L. E., Staudaher, F. M., "Subclutter Visibility Demonstration", *Technical Report RL-TR-92-21, Adaptive Sensors Incorporated*, March 1992
- [6] Bühring, W., Klemm, R., "Ein adaptives Filter zur Unterdrückung von Radarstörungen mit unbekanntem Spektrum" (An adaptive filter for suppression of clutter with unknown spectrum), *FREQUENZ*, Vol. 30, No. 9, September 1976, (in German), pp. 238-243
- [7] Coe, D. J., White, R. G., "Experimental moving target detection results from a three-beam airborne SAR", *AEU*, Vol. 50, No. 2, March 1996
- [8] Compton, R. T. jr., "The Bandwidth Performance of a Two-Element Adaptive Array with Tapped Delay-Line Processing", *IEEE Transaction on Antenna and Propagation*, Vol. AP-36, No. 1, January 1988, pp. 5-14
- [9] Compton, R. T. jr., "The Relationship Between Tapped Delay-Line and FFT Processing in Adaptive Arrays", *IEEE Transaction on Antenna and Propagation*, Vol. AP-36, No. 1, January 1988, pp. 15-26
- [10] Covault, C., "Space-based radars drive advanced sensor technologies", *Aviation Week & Space Technology*, April 5, 1999, pp. 49-50
- [11] Doherty, J. F., "Suppression of Terrain Scattered Jamming in Pulse Compression Radar", *IEEE Transactions on Signal Processing*, Vol. 2, No. 1, January 1995, pp. 4-6
- [12] Ender, J., "The airborne experimental multi-channel SAR system", *Proc. EUSAR '96*, 26-28 March 1996, Koenigswinter, Germany, pp. 49-52 (VDE Publishers)
- [13] Ender, J., "Detection and Estimation of Moving Target Signals by Multi-Channel SAR", *Proc. EUSAR '96*, 26-28 March 1996, Koenigswinter, Germany, pp. 411-417, (VDE Publishers)-Also: *AEU*, Vol. 50, March 1996, pp. 150-156
- [14] Ender, J., "Experimental results achieved with the airborne multi-channel SAR systems AER II. The airborne experimental multi-channel SAR system", *Proc. EUSAR '98*, 25-27 May 1998, Friedrichshafen, Germany
- [15] Farina, A., Timmoneri, L., "Space-time processing for AEW radar", *Proc. RADAR 92*, Brighton, UK, 1992, pp. 312-315
- [16] Gross, L.A., Holt, H.D., "AN/APY-6 realtime surveillance and targeting radara development", *Proc. NATO/IRIS Conference*, 19-23 October 1998, paper G-3
- [17] Haimovich, A. L., Bar-Ness, Y., "An Eigenanalysis Interference Canceler", *IEEE Trans. Signal Processing*, Vol. 39, No. 1, January 1991, pp. 76-84

- [18] Ayoub, T. F., Haimovich, A. M., Pugh, M. L., "Reduced-rank STAP for high PRF radar", *IEEE Trans. AES*, Vol. 35, No. 3, July 1999, pp. 953-962
- [19] Hippler, J., Fritsch, B., "Calibration of the Dornier SAR with trihedral corner reflectors", *Proc. EU-SAR '96*, 26-28 March 1996, Koenigswinter, Germany, pp. 499-503, (VDE Publishers)
- [20] Jouny, I. I., Culpepper, E., "Modeling and mitigation of terrain scattered interference", *IEEE Antennas and Propagation Symposium*, 18-23 June, 1995, Newport Beach, USA, pp. 455-458
- [21] Klemm, R., "Adaptive Clutter Suppression for Airborne Phased Array Radar", *Proc. IEE*, Vol. 130, No. 1, February 1983, pp. 125-132
- [22] Klemm, R., Ender, J., "New Aspects of Airborne MTI", *Proc. IEEE Radar 90*, Arlington, USA, 1990, pp. 335-340
- [23] Klemm, R., "Antenna design for airborne MTI", *Proc. Radar 92*, October 1992, Brighton, UK, pp. 296-299
- [24] Klemm, R., "Adaptive Airborne MTI: Comparison of Sideways and Forward Looking Radar", *IEEE International Radar Conference*, Alexandria, VA, May 1995, pp. 614-618
- [25] Klemm, R., ed., *Digest of the IEE Colloquium on STAP*, 6 April 1998, IEE, London, UK
- [26] Klemm, R., *Space-Time Adaptive Processing - Principles and Applications* IEE Publishers, London, UK, 1998)
- [27] Klemm, R., "Comparison between monostatic and bistatic antenna configurations for STAP", *IEEE Trans. AES*, April 2000
- [28] Klemm, R., (ed.), Special issue on "Space-Time Adaptive Processing", *IEE ECEJ*, February 1999
- [29] Klemm, R., "Space-time adaptive FIR filtering with staggered PRI", *ASAP 2001*, MIT Lincoln Lab., Lexington, MA, USA, 13-15 March 2001, pp.
- [30] Klemm, R., "Doppler properties of airborne clutter", *RTO SET Lecture Series 228* (this volume)
- [31] Koch, W., Klemm, R., "Ground target tracking with STAP radar", *IEE Proc. Radar, Sonar and Navigation*, 2001
- [32] Melvin, W. L., (ed.), Special issue on "Space-Time Adaptive Processing and Adaptive Arrays", *IEEE Trans. AES*, April 2000
- [33] Kreyenkamp, O., "Clutter covariance modelling for STAP in forward looking radar", *DGON International Radar Symposium 98*, September 15-17, 1998, München, Germany
- [34] Lee, F. W., Staudaher, F., "NRL Adaptive Array Flight Test Data Base", *Proc. of the IEEE Adaptive Antenna Systems Symposium*, Melville, New York, November 1992
- [35] Richardson, P. G., Hayward, S. D., "Adaptive Space-Time Processing for Forward Looking Radar", *Proc. IEEE International Radar Conference*, Alexandria, VA, USA, 1995, pp. 629-634
- [36] Richardson, P. G., "Effects of manoeuvre on space-time adaptive processing performance", *Proc. IEE Radar '97*, 14-16 October 1997, Edinburgh, Scotland, pp. 285-289
- [37] Sanyal, P. K., Brown, R. D., Little, M. O., Schneible, R. A., Wicks, M. C., "Space-time adaptive processing bistatic airborne radar", *IEEE National Radar Conference*, 20-22 April 1999, Boston, USA, pp. 114-118

- [38] Shnitkin, H., "A Unique JOINT STARS Phased Array Antenna", *Microwave Journal*, January 1991, pp. 131-141
- [39] Skolnik, M., *Radar Handbook*, 1st Ed., McGraw-Hill, New York, 1970
- [40] Tobin, M., "Real-Time Simultaneous SAR/GMTI in a Tactical Airborne Environment", *Proc. EUSAR '96*, 26-28 March, 1996, Koenigswinter, Germany, pp. 63-66, (VDE Publishers)
- [41] Titi, G. W., "An Overview of the ARPA/NAVY Mountaintop Program", *IEEE Adaptive Antenna Symposium*, Melville, New York November 7-8, 1994
- [42] Tsandoulas, G. N., "Unidimensionally Scanned Phased Arrays", *IEEE Trans. on Antennas and Propagation*, Vol. AP28, No. 1, November 1973, pp. 1383-1390
- [43] Wang, H., Cai, L., "On Adaptive Spatial-Temporal Processing for Airborne Surveillance Radar Systems", *IEEE Trans. AES*, Vol. 30, No. 3, July 1994, pp. 660-670
- [44] Wang Z., Bao Z., "A Novel Algorithm for Optimum and Adaptive Airborne Phased Arrays", *Proc. SITA '87*, 19-21 November 1987, Tokyo, Japan, pp. EE2-4-1
- [45] Wang, H., Zhang, Y., Zhang, Q., "An Improved and Affordable Space-Time Adaptive Processing Approach", *Proc. International Conference on Radar (ICR '96)*, Beijing, China, 8-10 October 1996, pp. 72-77
- [46] Ward, J., "Space-Time Adaptive Processing for Airborne Radar", *Technical Report No. 1015*, Lincoln Laboratory, MIT, December 1994
- [47] Ward, J., "Cramer-Rao Bounds for Target Angle and Doppler Estimation with Space-Time Adaptive Processing Radar", *Proc. 29th ASILOMAR Conference on Signals, Systems and Computers*, 30 October-2 November 1995, pp. 1198-1203